Energy Storage Materials 25 (2020) 76–85

Contents lists available at ScienceDirect

Energy Storage Materials

journal homepage: www.elsevier.com/locate/ensm

Surface Ni-rich engineering towards highly stable $Li_{1.2}Mn_{0.54}Ni_{0.13}Co_{0.13}O_2$ cathode materials

Hongfei Zheng [a], Zhenyu Hu [a], Pengfei Liu [a], Wanjie Xu [a], Qingshui Xie [a,**], Wei He [a], Qing Luo [a], Laisen Wang [a], DanDan Gu [b], Baihua Qu [b,***], Zi-Zhong Zhu [c], Dong-Liang Peng [a,*]

[a] State Key Lab of Physical Chemistry of Solid Surface, Collaborative Innovation Center of Chemistry for Energy Materials, College of Materials, Xiamen University, Xiamen, 361005, China
[b] Pen-Tung Sah Institute of Micro-Nano Science and Technology, Xiamen University, Xiamen, 361005, China
[c] Collaborative Innovation Centre for Optoelectronic Semiconductors and Efficient Devices, Department of Physics, Xiamen University, Xiamen, 361005, China

ARTICLE INFO

Keywords:
Ni-rich engineering
Li-rich layered oxides
Lithium ion battery cathode
Surface modification
Cycling stability

ABSTRACT

Li-rich layered oxide cathode materials (LLOs) are regarded as promising next-generation cathode candidate in high-energy-density lithium ion batteries due to their high specific capacity over 250 mA h g^{-1}. However, LLOs always suffer from a series of severe issues, such as rapid voltage fading, fast capacity decay and bad cycling stability. In this work, $Li_{1.2}Mn_{0.54}Ni_{0.13}Co_{0.13}O_2$-$Li_{1.2}Mn_{0.44}Ni_{0.32}Co_{0.04}O_2$ (LLO-111@111/811) hybrid layered-layered cathode is constructed via facilely increasing surface Ni content. Profiting from this special design, the prepared LLO-111@111/811 cathode exhibits a remarkable specific capacity of 249 mA h g^{-1} with a high capacity retention of 89.3% and a high discharge voltage of 3.57 V with a voltage retention of 83.0% after cycling 350 times at 0.5 C. As a result, the specific energy of LLO-111@111/811 cathode is 887 Wh Kg^{-1} at 0.5 C and it keeps as high as 658 Wh Kg^{-1} after 350 cycles. LLO-111@111/811 also exhibits an initial high capacity of 169 mA h g^{-1} at a high rate of 5 C and maintains a good capacity retention of 90.0% after 200 cycles. This strategy can successfully improve structural stability, suppress capacity decay and restrain voltage fading of LLOs, which is beneficial for their practical application.

1. Introduction

Research on rechargeable lithium ion batteries (LIBs) has made great progress in the past few decades and the LIBs have been widely used in electric vehicles and various portable electronics [1]. However, the specific energy of current LIBs based on graphite anode and classic oxide cathode materials such as layered $LiMO_2$ (M = Ni, Co, Mn), ternary $LiNi_xCo_yMn_zO_2$, $LiMn_2O_4$ and $LiFePO_4$ is less than 250 Wh kg^{-1} due to one of significant factors that is the limited theoretical capacity of these cathode materials [2,3]. In order to keep up with the ever-increasing demands for high-energy-density batteries, the lithium-rich layered oxide materials, Li_2MnO_3·$LiMO_2$ (M = Mn, Ni, Co), become the most promising candidates for their superior specific capacity over 250 mA h g^{-1} attributed to the additional capacity from the activation of Li_2MnO_3 in the first charging process [3,4]. Unfortunately, the activation process of lithium-rich layered oxide cathode materials (hereafter abbreviated as LLOs) is always accompanied by irreversible Li^+ extraction, oxygen release and the diffusion of transition ions into the Li layers, resulting in the structure transformation from layered to spinel phase and then fast voltage/capacity decay [5]. In addition, the LLOs suffer from low rate performance due to their intrinsic low lithium ionic conductivity of the Li_2MnO_3 phase [6,7].

To address these drawbacks, many strategies, such as micro/nanostructures design [8,9], concentration gradient construction [10], surface modification [11], doping [12], and morphology regulation [13], have been proposed. It is well established that the layered-to-spinel transformation occurs preferentially on the surface of LLOs, and some conventional surface coating materials, such as phosphates, fluorides, sulfides, metal oxides and so on, have been demonstrated great effectivity to protect surface from erosion of electrolyte under high voltage condition and then improve structure stability [14,15]. However, most coating materials are electrochemically inactive as well as bad electron or ion

* Corresponding author.
** Corresponding author.
*** Corresponding author.
E-mail addresses: xieqsh@xmu.edu.cn (Q. Xie), bhqu@xmu.edu.cn (B. Qu), dlpeng@xmu.edu.cn (D.-L. Peng).

https://doi.org/10.1016/j.ensm.2019.10.029
Received 29 August 2019; Received in revised form 14 October 2019; Accepted 26 October 2019
Available online 31 October 2019

conductors, which are bad for the specific capacity and rate performance of LLOs [16].

On this basis, constructing electrochemically active coating is significant. For example, spinel lithium oxides coatings are widely used to improve the electrochemical properties of the spinel-layered hybrid cathodes because of their offered certain electrochemical capacity and 3D Li^+ ions diffusion channels [17–20]. Some other hybrid layered-layered cathodes, such as $Li_{1.2}Mn_{0.54}Ni_{0.13}Co_{0.13}O_2$@x$LiNiO_2$ and $LiNi_{0.80}Co_{0.15}Al_{0.05}O_2$@ $Li_{1.2}Mn_{0.54}Ni_{0.13}Co_{0.13}O_2$ cathodes, have also been reported [21,22]. Another effective strategy is to construct nickel-increased LLOs, such as Ni-increased Ni/Mn-graded LLOs, $Li_{1.13}Ni_{0.26}Co_{0.09}Mn_{0.52}O_2$ and $Li_{1.2}Ni_{0.32}Co_{0.04}Mn_{0.44}O_2$, to remarkably mitigate voltage decay and improve cycle-life performances [10,22,23]. The improvement of electrochemical performances is attributed to two main factors [22,24]. One is that the properly increased nickel ions possess stabilizing effect to inhibit the Jahn-Teller effect of Mn^{3+}, improve d-p hybridization and support the layered structure as a pillar. The other is that nickel ions would migrate between the transition-metal layer and the interlayer to avoid the formation of spinel-like structures and consequently mitigate the voltage decay. However, the excess nickel ions would not only cause severe Ni^{2+}/Li^+ cation mixing that would lead to undeserved structure deterioration, but also decrease the theoretical specific capacity of cathode materials. Thus, it is great meaningful to regulate the Ni content on the surface region of LLOs material reasonably in order to effectively improve electrochemical performances, which still remains great challenge up to now.

Herein, a facile and reasonable one-step strategy is put forward to construct layered-layered hybrid cathode $Li_{1.2}Mn_{0.54}Ni_{0.13}Co_{0.13}O_2$-$Li_{1.2}Mn_{0.44}Ni_{0.32}Co_{0.04}O_2$ (LLO-111@111/811) via surface Ni-rich engineering, aiming to remain high specific capacity, improve structure stability and suppress capacity/voltage decay of LLOs simultaneously. The elaborately designed LLO-111@111/811 cathode material possesses the following merits. Firstly, LLO-111@111/811 exerts the advantages of high capacity of inner LLO-111 and high surface stability due to the surface modification of Ni-rich LLO-811, which is favorable for suppressing structural transitions and side-reactions on the electrode/electrolyte interface during repeated Li^+ deintercalation/intercalation processes. Secondly, both LLO-111 and LLO-811 materials possess layered structure, so there is no obvious boundary between the inner cathode material and surface hybrid material, which is good for Li^+ diffusion. Finally, the one-step strategy leaves out traditional additional coating process after successfully preparing LLOs, it is facile to operate and control in practical production and is favorable for avoiding impurity to reduce properties. As a consequence, the prepared LLO-111@111/811 exhibits a high reversible capacity, excellent cycling stability, good rate capability and enhanced voltage retention. It is worth mentioning that the specific energy output for LLO-111@111/811 is 887 Wh Kg^{-1} at 0.5 C and it keeps as high as 658 Wh Kg^{-1} after 350 cycles.

2. Experimental section

2.1. Material preparation

$LiCH_3COO{\cdot}2H_2O$, $Mn(CH_3COO)_2{\cdot}4H_2O$, $Co(CH_3COO)_2{\cdot}4H_2O$ and $Ni(CH_3COO)_2{\cdot}4H_2O$ with molar ratio of 1.32:0.54:0.13:0.13 were dissolved into ethanol solvent to obtain a ~0.4 M mixed solution A and those with molar ratio of 1.32:0.44:0.32:0.04 were dissolved into ethanol solvent to obtain a ~0.08 M mixed solution B. The metal ions ratio of solution B to solution A is ~1:9. The solution A was continuously stirred at 60 °C for 0.5 h under nitrogen atmosphere. Then 30 ml of oxalic acid (1 M) ethanol solution was added into the solution A drop by drop until complete co-precipitation. After aging for 3 h, the solution B was added drop by drop into the mixed metal-oxalate solution under magnetic stirring and aged for another 3 h. The solution mixture was transferred into a sealed Teflon-lined autoclave, followed by heating at 180 °C for 24 h. After the solvothermal reaction, the as-prepared precipitate was separated through centrifugal washing and then dried in a vacuum case at 80 °C for 12 h. The obtained precipitate was calcined at 500 °C for 4 h in air firstly, then at 800 °C for 10 h and finally at 900 °C for another 2 h to prepare the $Li_{1.2}Mn_{0.54}Ni_{0.13}Co_{0.13}O_2$-$Li_{1.2}Mn_{0.44}Ni_{0.32}Co_{0.04}O_2$ (LLO-111@111/811, the theoretical metal cation ratio of Mn: Ni: Co is 53:14.9:12.1). The LLO-111 and LLO-811 were also synthesized for comparison by the same method with metal cation molar ratio of 1.32:0.54:0.13:0.13 and 1.32:0.44:0.32:0.04 in solution A (no addition of solution B), respectively.

2.2. Material characterization

X-ray diffraction (XRD) was characterized on Rikagu Ultima IV equipped with a Cu Kα radiation source operating at 40 kV and 40 mA, the 2θ range was from 10 to 100° and the scan rate was 1° min^{-1}. Rietveld refinements of the XRD were carried out by General Structure Analysis System (GSAS) software. The X-ray photoelectron spectroscopy (XPS) was performed on a PHI Quantum 2000 Scanning ESCA Microprobe with an Al X-ray source. The morphology of the cathode materials was observed by scanning electron microscopy (SEM) of Hitachi SU-70. Transmission electron microscopy (TEM) images, high-angle annular dark field (HAADF) images, energy dispersive X-ray (EDX) spectroscopy, TEM-EDX elemental mapping, TEM-EDX elemental line-scanning and selected area electron diffraction (SAED) were performed on a TECNAI F-30 TEM operating at 300 kV and a Talos-200s TEM operating at 200 kV.

2.3. Electrochemical measurements

The electrochemical properties of the fabricated LLOs cathode materials were investigated by assembling CR2025-type coin cells in an argon-filled glovebox (moisture and oxygen contents below 0.1 ppm), with Li metal foil as the counter electrode and commercial polypropylene (PP) membrane (Celgard 2325) as the separator. The cathode slurry, consisting of 70 wt% of as-prepared material, 20 wt% of acetylene black, 10 wt% of polyvinylidene fluoride (PVDF) binder, was mixed in amount of N-methylpyrrolidone (NMP) organic solvent and then coated on Al foil uniformly. The electrodes were dried at 80 °C for 12 h under vacuum condition to prepare the working electrode before use. The electrolyte solution was 1 M $LiPF_6$ in a mixed solvent of ethylene carbonate (EC), ethyl methy carbonate (EMC), and dimethyl carbonate (DMC) (1:1:1 in volume). The cells were charged and discharged within the voltage range of 2.0–4.8 V (vs. Li/Li^+) on Neware battery testing system at 0.2 C in the initial cycle and 0.5 C, 1 C or 5 C in subsequent cycles (1 C = 250 mA g^{-1}). Cyclic voltammetry (CV, 2.0–4.8 V at scan rate of 0.1 mV s^{-1}) and electrochemical impedance spectroscopy (EIS, 100 KHz to 0.01 Hz) were collected on the CHI660C electrochemical workstation.

2.4. Details of calculations

All calculations were conducted on the base of Vienna ab initio simulation package (VASP) [25,26]. Projector augmented wave (PAW) methods and Perdew-Burke-Ernzerhof (PBE) exchange correlation functional were adopted [27–29]. All the ions are fully relaxed until total energy difference was less than 10^{-5} eV and residual forces were less than 0.05 eV/Å. A $2 \times 2 \times 1$ grid was sampled in the Brillouin zone by Monkhorst−Pack scheme [30]. Charge density difference was plotted by VESTA [31]. Oxygen vacancy formation energy were calculated by a reported formula [32].

3. Results and discussion

The LLO-111, LLO-111@111/811 and LLO-811 samples were successfully synthesized by facile solvothermal method and solid-state reaction. The synthetic process of LLO-111@111/811 sample is schematically illustrated in Fig. 1. Through adjusting the molar ratio of transition metal ions, LLO-111@111/811 sample with chemical

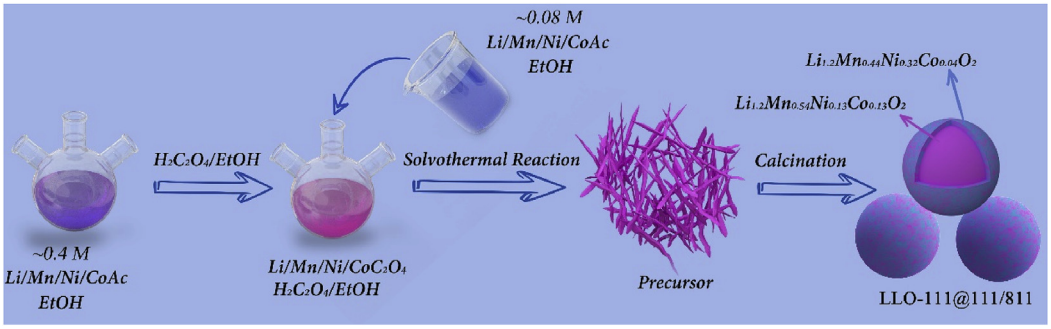

Fig. 1. Schematic illustration for the synthesis of LLO-111@111/811 cathode material.

composition difference inside and outside was synthesized. The morphologies of the LLO-111, LLO-111@111/811 and LLO-811 materials were characterized by SEM and TEM. As shown in Fig. 2 (a-c), all three samples exhibit similar morphology and are composed of primary particles with diameter of 150–500 nm, indicating that the surface Ni content regulation of sample does not affect the morphology of the final LLO-111@111/811. The 3D porous structure among primary particles and their small particle size would facilitate electrolyte penetration within the electrode and support a short pathway for rapid Li^+ ions diffusion, which benefits to accelerate deintercalation/intercalation rate of Li^+ ions [33]. The surface microstructures of the three LLOs were confirmed by high resolution TEM (HRTEM) as illustrated in Fig. 2 (d-f). It is obvious that the LLO-111 sample possesses a high degree of crystallization and the lattice fringes with a distance of 0.47 nm belong to the (003) plane of the layered phase [34]. By contrast, the HRTEM image of LLO-811 depicts that its crystallinity is not as good as LLO-111. The HRTEM image of LLO-111@111/811 reveals poor crystallographic layer on the surface but good crystallinity inside, which may be caused by more cation mixing due to the increased content of Ni on the surface. The elemental compositions of LLO-111, LLO-111@111/811 and LLO-811 materials were characterized by energy dispersive X-ray (EDX) spectroscopy in TEM as

Table 1
The molar ratios of Mn, Ni and Co elements in the LLO-111, LLO-811 and LLO-111@111/811 samples.

Samples	Mn	Ni	Co
LLO-111	54	12.78	14.00
LLO-811	44	32.81	3.88
LLO-111@111/811	53	14.95	12.44

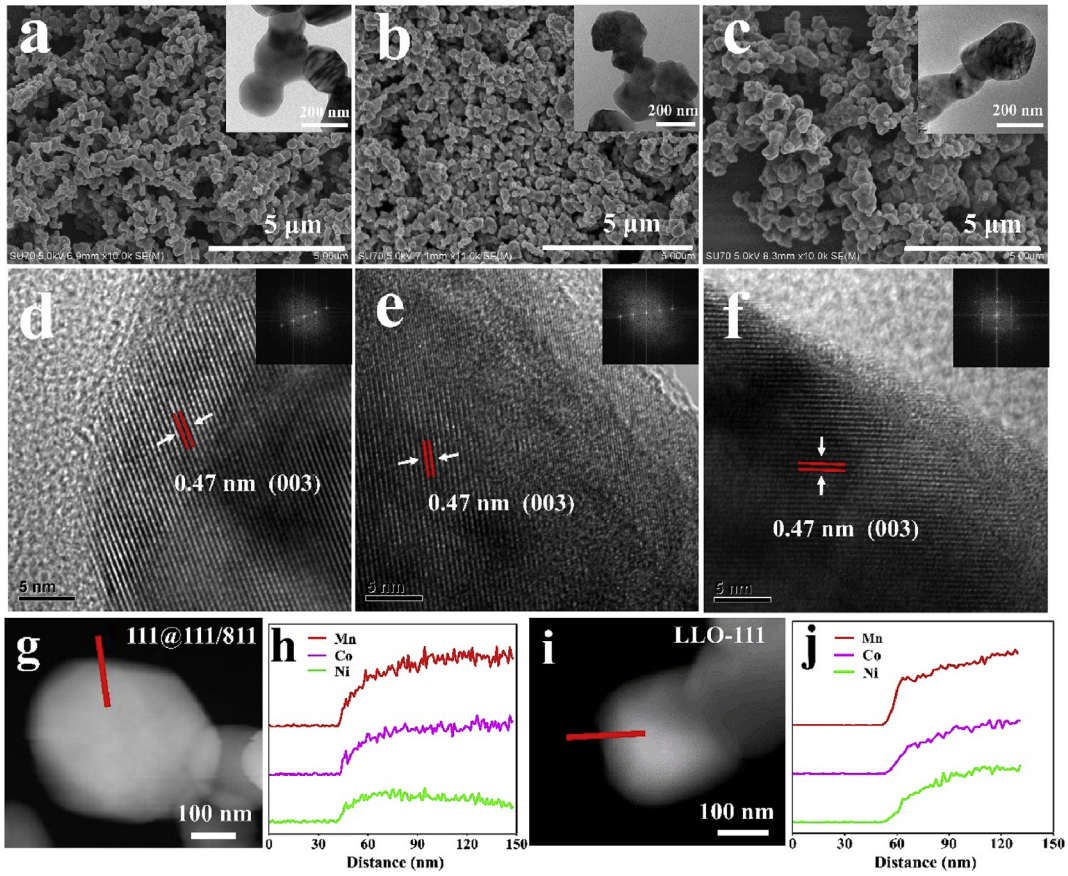

Fig. 2. SEM images of (a) LLO-111, (b) LLO-111@111/811 and (c) LLO-811. The insets in (a–c) are the corresponding TEM images. HRTEM images of (d) LLO-111, (e) LLO-111@111/811 and (f) LLO-811. The insets in (d–f) are the corresponding Fast Fourier Transform (FFT) patterns. (g) HAADF image of LLO-111@111/811 and (h) the corresponding STEM-EDX line-scanning image of Mn, Ni and Co elements. (i) HAADF image of LLO-111 and (j) the corresponding STEM-EDX line-scanning image.

shown in Table 1 and Fig. S1. The tabulated results indicate that the metal cation ratios of Mn: Ni: Co in LLO-111, LLO-811 and LLO-111@111/811 are well matched with the designed values (54:13:13 in LLO-111, 44:32:4 in LLO-811 and 53:14.9:12.1 in LLO-111@111/811).

To further disclose the high Ni content on the surface region in the as-prepared LLO-111@111/811 material, the surface elemental distribution was analyzed by STEM-EDX line scanning, the LLO-111 material was also tested for comparison. As shown in Fig. 2 (g-j), the contents of Mn, Co, and Ni elements in LLO-111@111/811 and LLO-111 were plotted as a function of distance from outside to inside around surface of a single particle. The high Ni content on the surface region but lower Ni content in the interior region can be observed in LLO-111@111/811, which is quite different with those of Mn and Co elements in LLO-111@111/811 and that of Ni element in LLO-111. In addition, EDX element mappings in Fig. S2 (d-e) show that the element distribution of Ni is rich and successive on the surface region of LLO-111@111/811, while that of Mn is barren and successive. These results confirm that the higher content of Ni has been successfully obtained on the surface of LLO-111@111/811.

To determine the phase structures, LLO-111, LLO-111@111/811 and LLO-811 cathode materials were identified by powder X-ray diffraction (XRD) as shown in Fig. 3 (a). LLO-111, LLO-811 and LLO-111@111/811 show main diffraction peaks from typical hexagonal α-$NaFeO_2$ structure with R-3m space group, which are attributed to the layered $LiMO_2$ component. The weak peaks located in the range of 20–25° are indexed to the super lattice of monoclinic Li_2MnO_3 (C2/m), resulting from the cation ordering of Li and transition metals (TMs) in the TM layer of the layered lattice, and are the characteristic of Li-rich layered oxides. As illustrated in Fig. 3 (a_1), the super lattice peaks of LLO-111 are the strongest while those of LLO-811 are the weakest, declaring the more content of Li_2MnO_3 phase in LLO-111 due to the higher Mn and lower Ni contents in LLO-111 compared with LLO-811. In Fig. 3 (a_2), the distinct peak splitting between the adjacent peaks of (018)/(110) in LLO-111 and LLO-111@111/811 verifies their good layered structure. However, the (018)/(110) peak splitting in LLO-811 is not obvious, indicating more obvious cation mixing due to its high Ni content. The intensity ratio of (003)/(104) peaks for LLO-811 is 1.15 (less than 1.2), suggesting that cation mixing takes place. For LLO-111 and LLO-111@111/811, the intensity ratios of the (003)/(104) peaks are both bigger than 1.32, further validating their good layered structure.

To obtain more accurate crystallographic information, Rietveld refinements of the XRD patterns with full spectrum fitting data for LLO-111, LLO-111@111/811 and LLO-811 were conducted by GSAS program. The results are illustrated in Fig. 3 (b), Fig. S3 (a-b) and Table S1. LLO-111 possesses the highest content of Li_2MnO_3 (31.0 wt%), which is higher than those of LLO-111@111/811 (20.6 wt%) and LLO-811 (11.4 wt%). In addition, the degree of cation mixing in LLO-111 (3.6%) is the lowest compared with LLO-111@111/811 (4.2%) and LLO-811 (5.7%).

The Raman spectra of LLO-111, LLO-111@111/811 and LLO-811 are shown in Fig. S3 (c). Two obvious peaks can be found at 494 and 604 cm^{-1} for all three LLO samples, which represent the E_g and stretching A_{1g} modes in the R-3m layered structure, respectively. Moreover, some narrow and weak peaks around 320-440 cm^{-1} are observed and ascribed to the fingerprint vibration of C2/m layered structure.

The surface valence states and the surface chemistry of LLO-111, LLO-111@111/811 and LLO-811 were tested by XPS and the results are presented in Fig. 3 (c-d) and Fig. S3 (d-e). The XPS full spectra in Fig. S3 (d) confirm the existence of Ni, Co, Mn, O, C and Li elements in these three samples and no other elements can be found. In terms of LLO-111@111/811 material, the dominant binding energy peaks of Ni $2p_{3/2}$, Co $2p_{3/2}$ and Mn $2p_{3/2}$ locate at 855.4, 780.5 and 642.7 eV, respectively, which coincide well with Ni^{2+}, Co^{3+} and Mn^{4+} ions [35,36]. As shown in Fig. 3 (c-d), almost no peak shift of Ni $2p_{3/2}$ and Co $2p_{3/2}$ can be found among LLO-111, LLO-111@111/811 and LLO-811, however, their intensity are different. The intensity of Ni $2p_{3/2}$ in LLO-111@111/811 is stronger than LLO-111 and lower than LLO-811, and LLO-811 exhibits the lowest intensity of Co $2p_{3/2}$. These phenomena are attributed to the difference contents of Ni and Co elements in these samples. In Fig. S3 (e), the peak positions of Mn $2p_{1/2}$ and Mn $2p_{3/2}$ gradually shift to higher binding energy from LLO-111, LLO-111@111/811 to LLO-811, corresponding to the gradually increased content of higher average chemical valence of Mn ions [37]. All above results indicate that Ni-rich surface engineering in LLO-111@111/811 has been successfully carried out.

The electrochemical performances of LLO-111, LLO-111@111/811 and LLO-811 cathode materials were tested from 2.0 V to 4.8 V. Fig. 4 (a) illustrates the initial galvanostatic charge and discharge profiles of LLO-111, LLO-111@111/811 and LLO-811 at 0.2 C. All three cathodes exhibit typical characteristics of Li-rich oxides. The initial charge curves for all three samples are composed of a sloping curve below 4.45 V and a long

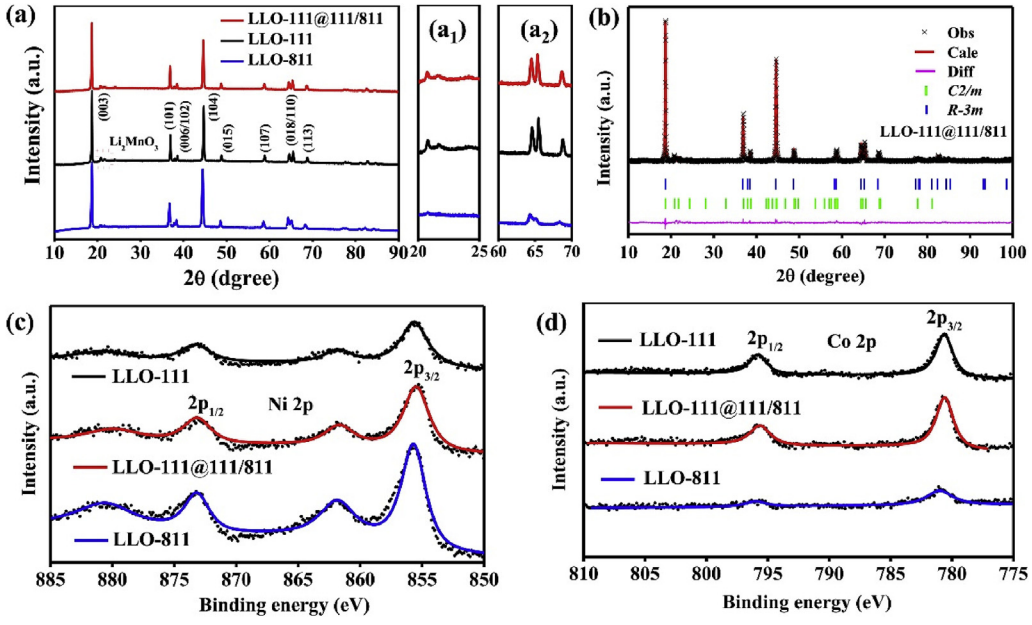

Fig. 3. (a) Powder XRD patterns of LLO-111, LLO-111@111/811 and LLO-811, (a_1-a_2) insets took out from (a). (b) Rietveld refinement of the XRD data of LLO-111@111/811. (c) Ni 2p and (d) Co 2p high-resolution XPS spectra of LLO-111, LLO-111@111/811 and LLO-811.

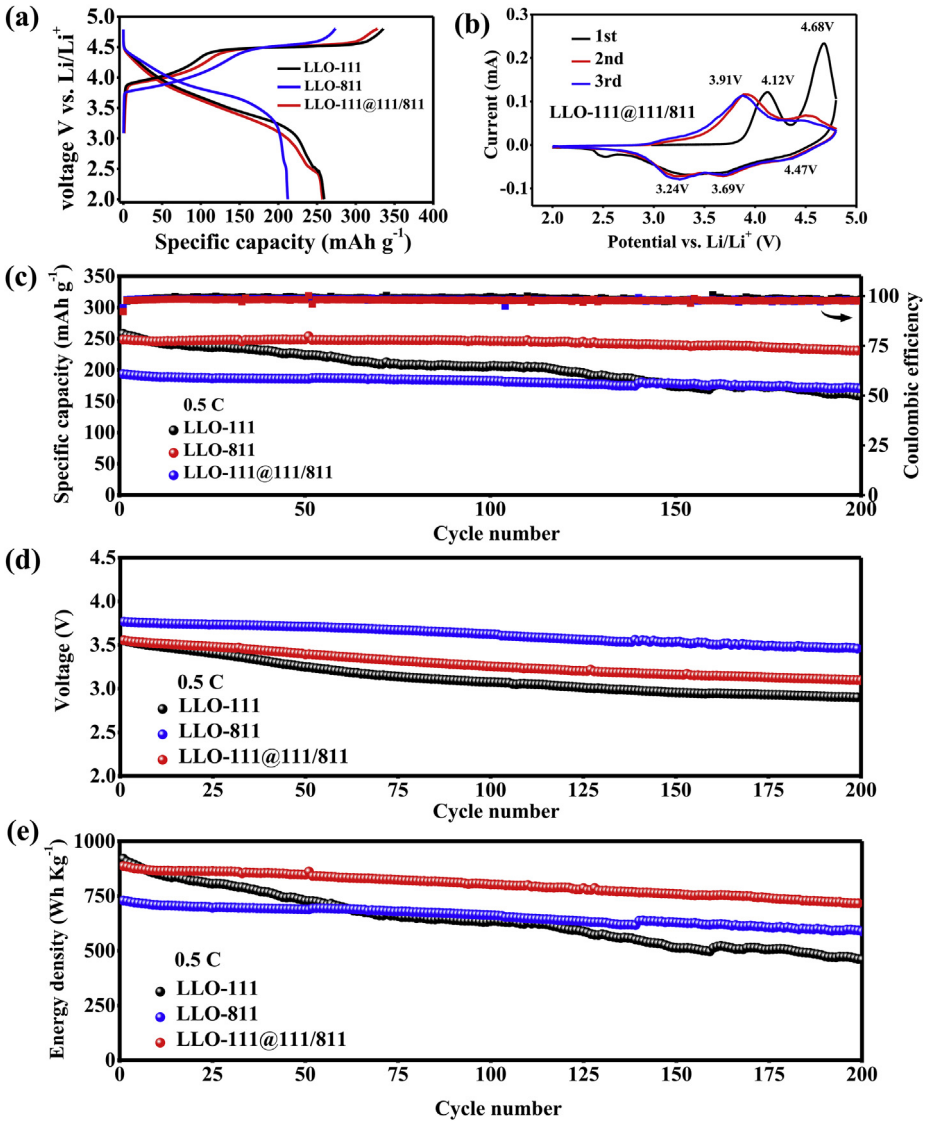

Fig. 4. (a) The initial galvanostatic charge/discharge profiles of LLO-111, LLO-111@111/811 and LLO-811, (b) the first three cyclic voltammogram curves (CV) of LLO-111@111/811. (c–e) cycling performances of LLO-111, LLO-111@111/811 and LLO-811 at 0.5 C, all cells were first activated at 0.2 C.

plateau around 4.5 V. The slope curve is ascribed to the Li^+ extraction from the layered $LiMO_2$ structure, during which the oxidation reactions of $Ni^{2+}/Ni^{3+}/Ni^{4+}$ and Co^{3+}/Co^{4+} occur [11,38]. The long plateau is attributed to the activation of the Li_2MnO_3 phase, accompanied by Li^+ extraction, oxygen release, and the TM ion diffusion into the Li layers [39]. As tabulated in Table 2, the charge capacity of sloping region below 4.45 V increases and that of long plateau from 4.45 to 4.55 V decreases with gradually increasing Ni content from LLO-111, LLO-111@111/811 to LLO-811, which supports forceful evidence that the content of layered $LiMO_2$ phase increases and that of Li_2MnO_3 phase decreases as a result of the increased Ni content. These results are in accordance with above Rietveld refinement data. The initial charge/discharge capacities are 335.5/259.2, 327.1/257.1, and 273.5/212.2 mA h g^{-1} for LLO-111, LLO-111@111/811 and LLO-811, respectively, showing that the regulation of surface Ni-rich chemical composition of LLO-111@111/811 nearly wouldn't reduce its capacity.

The electrochemical redox reactions of the three LLOs cathodes during cycling were investigated by cyclic voltammetry (CV) from 2.0 V to 4.8 V and the results are revealed in Fig. 4 (b) and Fig. S4. LLO-111@111/811 exhibits two obvious oxidation peaks around 4.12 and 4.68 V in the first anodic reaction. The peak around 4.12 V is related to the deintercalation of Li^+ ions from $LiMO_2$ component, accompanying by the oxidation of Ni^{2+} to Ni^{4+} and Co^{3+} to Co^{4+} [23]. The second peak around 4.68 V can be attributed to removal of Li^+ and the release of oxygen from Li_2MnO_3, thus leading to the formation of MnO_2 component [40]. In the cathodic process, one weak peak at 4.47 V and two main

Table 2
The initial charge/discharge capacities of LLO-111, LLO-111@111/811 and LLO-811 cathode materials at 0.2C.

Samples	Charge capacity below 4.45 V (mA h g^{-1})	Charge capacity from 4.45 to 4.55 V (mA h g^{-1})	Charge capacity (mA h g^{-1})	Discharge capacity (mA h g^{-1})
LLO-111	128.4	170.2	335.5	259.2
LLO-111@111/811	142.9	132.4	327.1	257.1
LLO-811	163.5	64.0	273.5	212.2

peaks at 3.69 and 3.24 V are discerned in LLO-111@111/811, corresponding to the reduction of Co^{4+} to Co^{3+}, Ni^{4+} to Ni^{2+} and Mn^{4+} to Mn^{3+}, respectively [8,41,42]. The peaks related to the oxidation reactions of Co^{3+}/Co^{4+} and $Ni^{2+}/Ni^{3+}/Ni^{4+}$ and the activation reaction of Li_2MnO_3 can be found at 4.05 and 4.61 V in LLO-111 as well as at 4.41 and 4.77 V in LLO-811. However, their intensity and peak position are different from those of LLO-111@111/811. With the content of Ni increasing, the oxidation peaks positions gradually shift to higher voltage, meanwhile, the intensity of oxidation peak of $Ni^{2+}/Ni^{3+}/Ni^{4+}$ gradually increases but that of oxidation peak related to the activation reaction of Li_2MnO_3 decreases, which coincides with the different charge capacities from the sloping curve and the long plateau demonstrated in Table 2. In addition, the reduction peaks corresponding to Co^{4+}/Co^{3+} and $Ni^{4+}/Ni^{3+}/Ni^{2+}$ in LLO-111 and the reduction peak corresponding to Mn^{4+}/Mn^{3+} in LLO-811 are too weak due to high Mn content in LLO-111 and high Ni content in LLO-811, respectively. With the Ni content increasing from LLO-111 (Fig. S4 (a)) to LLO-811 (Fig. S4 (b)), the reduction peak intensity related to $Ni^{4+}/Ni^{3+}/Ni^{2+}$ gradually increases and the discharge voltage is enhanced due to the positive effect of Ni ions. Ni ions not only present higher electronegativity than Mn ions under the same oxidation environment, but also can effectively regulate the local electronic structure, so substituting the Mn ions by Ni ions can efficiently improve the operating voltage and suppress voltage decay [43–45].

The cycling performances of LLO-111, LLO-111@111/811 and LLO-811 cathodes are tested after initial activation at 0.2 C for one cycle, and the results are showed in Fig. 4 (c-e) and Fig. 5 (a-c). LLO-111 cathode exhibits a high reversible discharge capacity of 258 mA h g^{-1} at 0.5 C at first cycle but its capacity retention is only 61.8% after 200 cycles, evidencing high specific capacity but rapid capacity decay (Fig. 4 (c)). Benefited from stabilizing effect of the increased Ni content in LLO-811, it exhibits a reversible discharge capacity of 194 mA h g^{-1} at 0.5 C at first cycle and its capacity retention is 88.4% after 200 cycles, showing low specific capacity but good electrochemical stability. Through integrating the high reversible capacity of LLO-111 and high cycling stability of LLO-811, the designed LLO-111@111/811 hybrid cathode exhibits not only high capacity of 249 mA h g^{-1} at 0.5 C at first cycle but high capacity retention of 93.0% after cycling 200 times. Meanwhile, the LLO-111@111/811 electrode exhibits a high discharge voltage of 3.57 V with a voltage retention of 87% after 200 cycles benefited from the higher discharge voltage due to the surface Ni-rich regulation, which is better than LLO-111 counterpart (Fig. 4 (d)). As a result, the initial specific energy of LLO-111@111/811 is 887 Wh Kg^{-1} at 0.5 C and it keeps as high as 717 Wh Kg^{-1} with a high retention of 80.8% after 200 cycles. However, the specific energy output is just 462.5 Wh Kg^{-1} with a low retention of 50.2% for LLO-111 and 593.3 Wh Kg^{-1} with a retention of 81.3% for LLO-811 after 200 cycles (Fig. 4 (e)). From Fig. 4 (c-e), LLO-111@111/811 possesses higher capacity and voltage retentions than pristine LLO-111, indicating effective improvement in capacity and voltage retention through surface Ni-rich engineering.

When cycled at 1 C, LLO-111@111/811 also shows good cyclability and delivers a high capacity of 214 mA h g^{-1} after 200 cycles (Fig. 5 (a)), which is much higher than those of LLO-111 (159 mA h g^{-1}) and LLO-811 (168 mA h g^{-1}) counterparts. The capacity retentions of LLO-111, LLO-111@111/811 and LLO-811 are 65.3%, 92.3% and 92.1%, respectively. The first CEs of LLO-111, LLO-111@111/811 and LLO-811 are 87.4%, 87.1% and 85.3% at 1 C, respectively. Then they are almost 100% in the following cycles. In addition, LLO-111@111/811 also exhibits high specific energy of 814.2 Wh Kg^{-1} at 1 C and it keeps as high as 652.1 Wh Kg^{-1} with a high retention of 80.1% after 200 cycles, preceding LLO-111 and LLO-811 (Fig. 5 (b)). As depicted in Fig. S4 (c), LLO-111@111/811 exhibits good rate performance. The discharge capacities

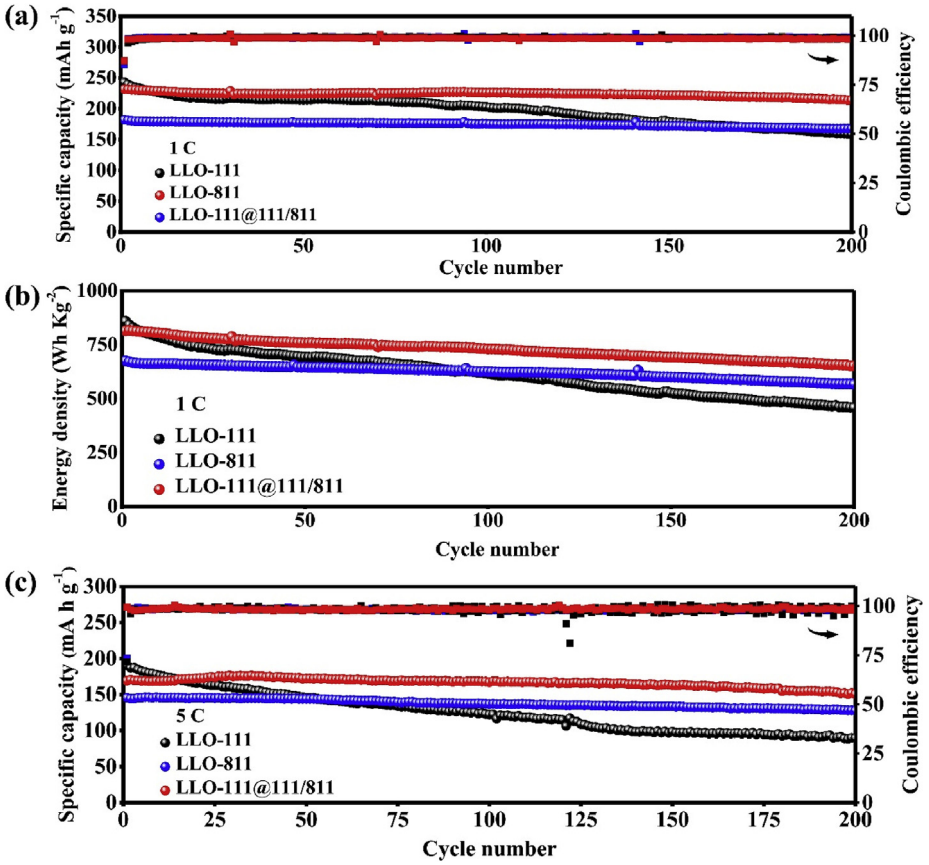

Fig. 5. (a–b) Cycling performances and the corresponding Coulombic efficiencies of LLO-111, LLO-111@111/811 and LLO-811 at 1 C and (c) cycling performances and the corresponding Coulombic efficiencies of LLO-111@111/811 at high rate of 5 C. All cells were first activated at 0.2 C.

of LLO-111@111/811 cathode are 258, 240, 223, 207 and 183 mA h g^{-1} at 0.2, 0.5, 1, 2 and 5 C, respectively. When the current density returns to 0.2 C, its discharge capacity can recover to 258 mA h g^{-1}. When cycled at a large current density of 5 C, the LLO-111@111/811 also shows good cyclability and delivers a high capacity of 152 mA h g^{-1} after 200 cycles, which is much higher than those of LLO-111 (90 mA h g^{-1}) and LLO-811 (128 mA h g^{-1}) counterparts. The capacity retentions of LLO-111, LLO-111@111/811 and LLO-811 are 47.2%, 90.0% and 88.1%, respectively. Furthermore, CEs of LLO-111@111/811 during long-term cycling are more stable than those of LLO-111(Fig. 5 (c)). The above results confirm the feasibility by constructing hybrid layered-layered LLO-111@111/811 cathode material via surface Ni-rich engineering to improve cycling stability and voltage retention simultaneously.

The impact of higher nickel ions on the voltage-stability was further verified by density functional theory (DFT) calculations. A reported mode was adopted as the low-nickel mode, and the high-nickel mode was gotten by doping extra nickel ions in lithium slabs in the low-nickel mode [46]. The site of the oxygen vacancy are illustrated in Fig. 6 (a). In the low-nickel mode, lattice oxygen tends to bond with the adjacent manganese ions in the transition metal slabs as shown in Fig. 6 (b). However, in the high-nickel content mode, an extra Ni-O bond will form between the nickel ions in lithium slabs and the lattice oxygen (Fig. 6 (c)). Thus, high-nickel mode has a higher oxygen vacancy formation energy than the low-nickel mode. Therefore, extra nickel ions in LLOs can stabilize lattice oxygen and maintain the voltage stability during electrochemical process, which is in accordance with the above experiments.

To further verify the good structural stability of LLO-111@111/811 electrode material, the in-situ XRD was performed during charge/discharge processes for first three cycles at 0.2 C and shown in Fig. 6 (d). Except (003), (101) and (104) peaks (marked by black star) originating from the LLO-111@111/811, all of the other peaks can be indexed as Al current collector, Be window and other materials in the electrode. During the first charging process to 4.8 V, the (101) and (104) peaks shift to high angle due to the extraction of Li^+ ions. While discharging from 4.8 to 2 V, the two peaks shift to low angle and returns to their original positions owing to the reversible insertion of Li^+ ions [47]. The (003) peak of LLO-111@111/811 exhibits slight peak shift and intensity change during charge/discharge processes. The change trends of (003), (101) and (104) peaks during the second and third cycles are similar to those in the first cycle. In-situ XRD results show the good structural reversibility and stability of LLO-111@111/811 cathode material during the Li^+ insertion and extraction processes [24,48].

Moreover, the LLO-111@111/811 cell was disassembled after cycling 222 times at 0.5 C and the active material was taken out and used as cathode again to pair with new Li foil for reassembling new cell. The new cell was subsequently tested at the same rate of 0.5 C (after 222nd cycles). Interestingly, the tendency of capacity decay after 160 cycles can be suppressed as shown in Fig. 7 (a) inset. Besides, the discharge capacity can be recovered from 223 mA h g^{-1} at 222nd cycle to 242 mA h g^{-1} at 240th cycle. As illustrated in Fig. 7 (b-c), this phenomenon is probably induced by the formation of Li dendrites on the Li foil surface during cycling, which would lead to capacity decay [49]. After changing the Li foil, LLO-111@111/811 delivers a high capacity of 222 mA h g^{-1} after total 350 cycles with a high retention of 89.3%. Thus, the rational conclusion can be drawn that the capacity decay of LLO-111@111/811 cell is mainly caused by the formation of Li dendrites, further confirming its good structure stability and good cyclability. In addition, LLO-111@111/811 delivers a high discharge voltage of 2.96 V even after 350 cycles with a high retention of 83%.

To further evaluate the structural stability of LLO-111 and LLO-111@111/811 cathode materials, the cathode materials after 200 cycles at 1 C were taken out after disassembling the cells for TEM investigation. From Fig. 8 (a), LLO-111@111/811 still maintains good surface stability compared with Fig. 2 (h). However, LLO-111 exhibits an apparently uneven surface and its surface has obvious cracks as displayed in Fig. 8 (c-d), which is attributed to the electrolyte erosion during

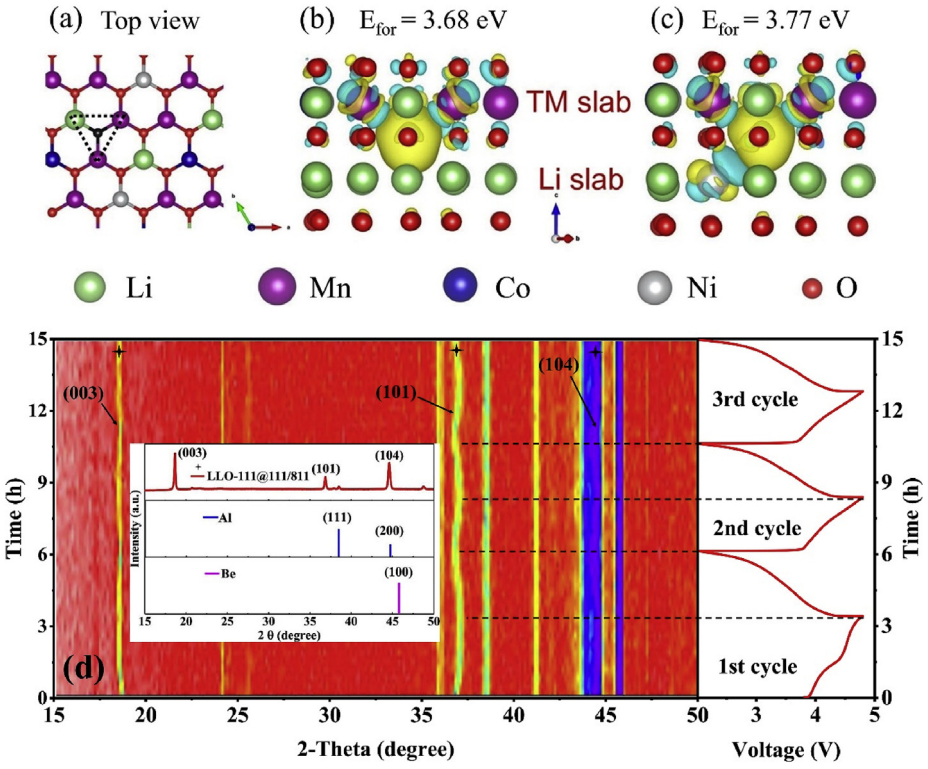

Fig. 6. (a) The site of the oxygen vacancy. Charge density difference and oxygen vacancy formation energy of (b) the low-nickel mode and (c) the high-nickel mode. (d) In-situ (003), (101) and (104) peaks evolution of LLO-111@111/811 and the corresponding charge/discharge curves at 0.2 C (2.0–4.8 V), where the value of intensity changes from 0 (red) to 360 (blue). (For interpretation of the references to colour in this figure legend, the reader is referred to the Web version of this article).

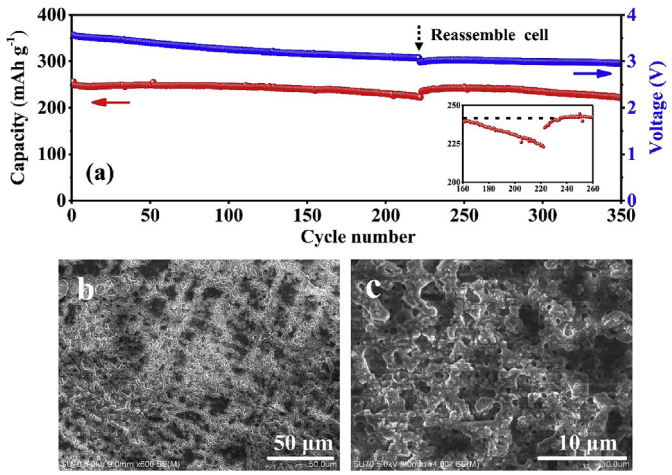

Fig. 7. (a) Long-term cycling performance of LLO-111@111/811 cathode at 0.5 C, (b–c) SEM images of the surface of Li foil counter electrode after 220 cycles at 0.5 C in LLO-111@111/811 half cell.

cycling and the resultant dissolution of the transition metal ions [50,51]. From Fig. 8 (d_1-d_2), it is clear that the surface of LLO-111 material after cycling exhibits a large amount of local erosion domains and the structural failure domains (lattice distortions or amorphous domains), which is closely associated with the capacity fading due to the electrochemically inactive characteristic of destroyed structure [11]. The SAED pattern features halo dots with an intensity fluctuation (Fig. 8 (e)), which indicates poor crystallinity of LLO-111 after cycling due to the severe structure decay, but the LLO-111@111/811 still exhibits good crystallinity (Fig. 8 (b) and Fig. S5) [52–54]. Fig. S6 further reinforce the conclusion that the structural stability of LLO-111@111/811 is superior to LLO-111.

The electrochemical impedance spectra (EIS) of LLO-111, LLO-111@111/811 and LLO-811 electrodes were measured and manifested in Fig. 9(a–b). The semicircle in high frequency region is connected with the interfacial charge transfer resistance (R_{ct}) [55,56]. The fitting equivalent circuit and the values of impedance parameters are shown in Fig. S7 and Table S2. For LLO-111, LLO-811 and LLO-111@111/811, R_{ct} values are 152.7, 146.9 and 109.4 Ω before cycling, however, R'_{ct} values are 255.2, 147.4 and 114.1 after 200 cycles. The change of interfacial charge transfer resistance in LLO-111@111/811 is the smallest among three

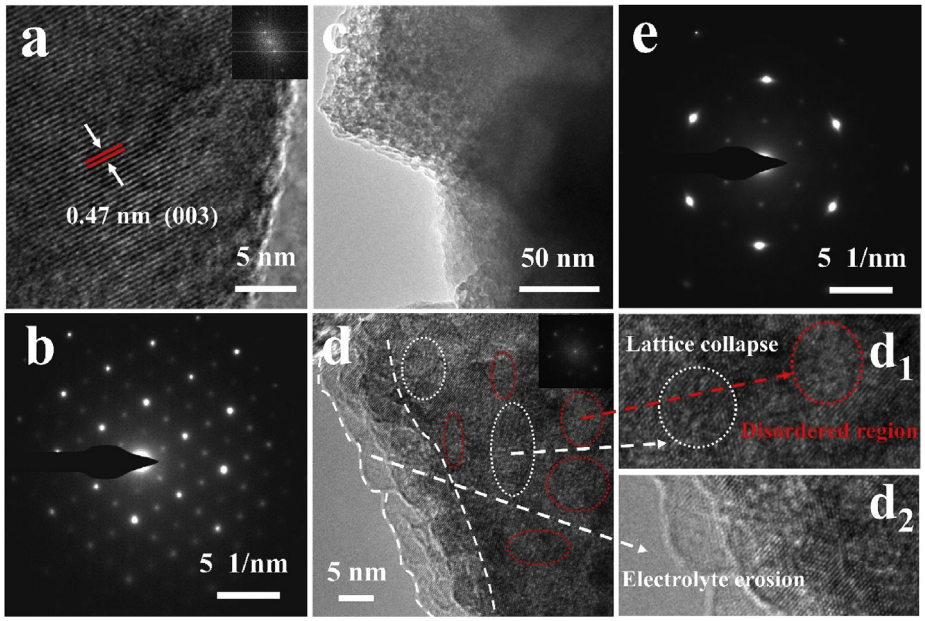

Fig. 8. (a) HRTEM image and (b) SAED image of LLO-111@111/811 after 200 cycles at 1 C. (c) TEM image, (d, d_1, d_2) corresponding HRTEM images and (e) SAED image of LLO-111 after 200 cycles at 1 C.

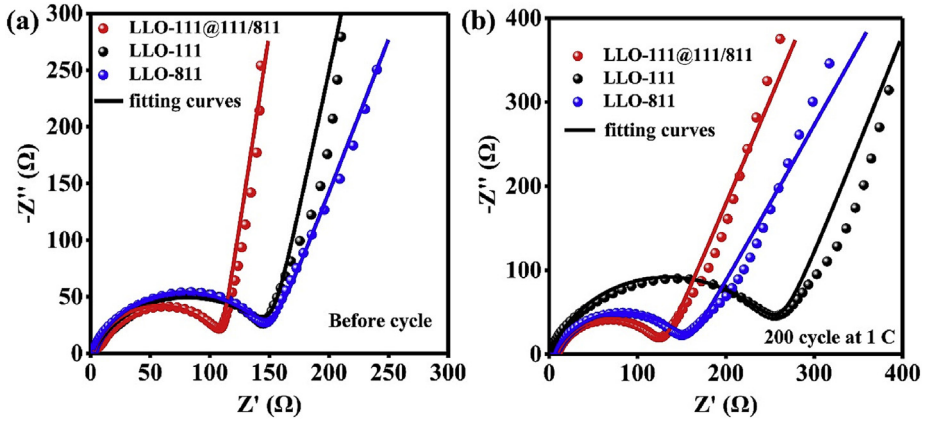

Fig. 9. EIS plots of LLO-111, LLO-111@111/811 and LLO-811 cathodes (a) before cycling and (b) after 200th cycles at 1 C.

samples, indicating its good interfacial stability. These results manifest the evident protective effect of surface Ni-rich engineering in LLO-111@111/811 cathode material, which can achieve high crystal structure stability during cycling and suppress the erosion of electrolyte, thus benefitting to enhance the capacity and voltage retentions.

4. Conclusion

In this work, hybrid layered-layered $Li_{1.2}Mn_{0.54}Ni_{0.13}Co_{0.13}O_2$-$Li_{1.2}Mn_{0.44}Ni_{0.32}Co_{0.04}O_2$ (LLO-111@111/811) cathode has been constructed via facile surface Ni-rich engineering. This strategy can effectively improve structure stability, suppress capacity and voltage decay of LLOs because the surface Ni-rich LLO-811 is favorable for restraining structural transitions and side-reactions on the electrode/electrolyte interface during cycling. As a consequence, the LLO-111@111/811 cathode exerts the advantages of high capacity of LLO-111 and high stability of LLO-811 simultaneously, resulting in large capacity of 249 mA h g^{-1} at 0.5 C with a high capacity retention of 89.3% as well as high discharge voltage of 3.57 V with a voltage retention of 83% after 350 cycles. Thus, the specific energy of LLO-111@111/811 is 887 Wh Kg^{-1} and keeps 658 Wh Kg^{-1} after cycling 350 times. It is demonstrated that the strategy of regulating surface chemical composition is beneficial for improving electrochemical performances of the Li-rich Mn-based layered cathode materials and may be extended to synthesize other advanced cathode materials for next-generation high-energy lithium ion batteries.

Declaration of competing interest

We wish to confirm that there are no known conflicts of interest associated with this publication and there has been no significant financial support for this work that could have influenced its outcome.

Acknowledgements

The authors gratefully acknowledge financial support from the National Natural Science Foundation of China (Grant Nos. 51931006, 51701169 and 51871188), the National Key R&D Program of China (Grant No. 2016YFA0202602), the Natural Science Foundation of Fujian Province of China (Nos. 2019J06003 and 2017J05087), the Key Projects of Youth Natural Foundation for the Universities of Fujian Province of China (No. JZ160397), the Fundamental Research Funds for the Central Universities of China (Xiamen University: Nos. 20720190007 and 20720190013) and the “Double-First Class” Foundation of Materials Intelligent Manufacturing Discipline of Xiamen University.

Appendix A. Supplementary data

Supplementary data to this article can be found online at https://doi.org/10.1016/j.ensm.2019.10.029.

References

[1] M. Li, J. Lu, Z. Chen, K. Amine, 30 Years of lithium-ion batteries, Adv. Mater. 30 (2018) 1800561.
[2] S. Chu, Y. Cui, N. Liu, The path towards sustainable energy, Nat. Mater. 16 (2016) 16–22.
[3] P.K. Nayak, E.M. Erickson, F. Schipper, T.R. Penki, N. Munichandraiah, P. Adelhelm, H. Sclar, F. Amalraj, B. Markovsky, D. Aurbach, Review on challenges and recent advances in the electrochemical performance of high capacity Li- and Mn-rich cathode materials for Li-ion batteries, Adv. Energy Mater. 8 (2018) 1702397.
[4] K.C. Jiang, X.L. Wu, Y.X. Yin, J.S. Lee, J. Kim, Y.G. Guo, Superior hybrid cathode material containing lithium-excess layered material and graphene for lithium-ion batteries, ACS Appl. Mater. Interfaces 4 (2012) 4858–4863.
[5] D. Ye, G. Zeng, K. Nogita, K. Ozawa, M. Hankel, D.J. Searles, L. Wang, Understanding the origin of Li_2MnO_3 activation in Li-rich cathode materials for lithium-ion batteries, Adv. Funct. Mater. 25 (2015) 7488–7496.
[6] S.K. Martha, J. Nanda, Y. Kim, R.R. Unocic, S. Pannala, N.J. Dudney, Solid electrolyte coated high voltage layered–layered lithium-rich composite cathode: $Li_{1.2}Mn_{0.525}Ni_{0.175}Co_{0.1}O_2$, J. Mater. Chem. 1 (2013) 5587–5595.
[7] J.M. Zheng, S.J. Myeong, W.R. Cho, P.F. Yan, J. Xiao, C.M. Wang, J. Cho, J.G. Zhang, Li- and Mn-rich cathode materials: challenges to commercialization, Adv. Energy Mater. 7 (2017) 1601284.
[8] Y. Ma, P. Liu, Q. Xie, G. Zhang, H. Zheng, Y. Cai, Z. Li, L. Wang, Z.-Z. Zhu, L. Mai, D.-L. Peng, Double-shell Li-rich layered oxide hollow microspheres with sandwich-like carbon@spinel@layered@spinel@carbon shells as high-rate lithium ion battery cathode, Nano Energy 59 (2019) 184–196.
[9] M. Xu, L. Fei, W. Zhang, T. Li, W. Lu, N. Zhang, Y. Lai, Z. Zhang, J. Fang, K. Zhang, J. Li, H. Huang, Tailoring anisotropic Li-ion transport tunnels on orthogonally arranged Li-rich layered oxide nanoplates toward high-performance Li-ion batteries, Nano Lett. 17 (2017) 1670–1677.
[10] F. Li, Y. Wang, S. Gao, P. Hou, L. Zhang, Mitigating the capacity and voltage decay of lithium-rich layered oxide cathodes by fabricating Ni/Mn graded surface, J. Mater. Chem. 5 (2017) 24758–24766.
[11] F. Ding, J. Li, F. Deng, G. Xu, Y. Liu, K. Yang, F. Kang, Surface heterostructure induced by $PrPO_4$ modification in $Li_{1.2}[Mn_{0.54}Ni_{0.13}Co_{0.13}]O_2$ cathode material for high-performance lithium-ion batteries with mitigating voltage decay, ACS Appl. Mater. Interfaces 9 (2017) 27936–27945.
[12] R.-P. Qing, J.-L. Shi, D.-D. Xiao, X.-D. Zhang, Y.-X. Yin, Y.-B. Zhai, L. Gu, Y.-G. Guo, Enhancing the kinetics of Li-rich cathode materials through the pinning effects of gradient surface Na^+ doping, Adv. Energy Mater. 6 (2016) 1501914.
[13] G. Ma, S. Li, W. Zhang, Z. Yang, S. Liu, X. Fan, F. Chen, Y. Tian, W. Zhang, S. Yang, M. Li, A general and mild approach to controllable preparation of manganese-based micro- and nanostructured bars for high performance lithium-ion batteries, Angew. Chem. Int. Ed. 55 (2016) 3667–3671.
[14] S. Zhang, H. Gu, T. Tang, W. Du, M. Gao, Y. Liu, D. Jian, H. Pan, In situ encapsulation of the nanoscale Er_2O_3 phase to drastically suppress voltage fading and capacity degradation of a Li- and Mn-rich layered oxide cathode for lithium ion batteries, ACS Appl. Mater. Interfaces 9 (2017) 33863–33875.
[15] W. Wei, L. Chen, A. Pan, D.G. Ivey, Roles of surface structure and chemistry on electrochemical processes in lithium-rich layered oxide cathodes, Nano Energy 30 (2016) 580–602.
[16] B. Wu, X. Yang, X. Jiang, Y. Zhang, H. Shu, P. Gao, L. Liu, X. Wang, Synchronous tailoring surface structure and chemical composition of Li-Rich-Layered oxide for high-energy lithium-ion batteries, Adv. Funct. Mater. 28 (2018) 1803392.
[17] A. Bhaskar, S. Krueger, V. Siozios, J. Li, S. Nowak, M. Winter, Synthesis and characterization of high-energy, high-power spinel-layered composite cathode materials for lithium-ion batteries, Adv. Energy Mater. 5 (2015) 1401156.
[18] Q. Xia, X. Zhao, M. Xu, Z. Ding, J. Liu, L. Chen, D.G. Ivey, W. Wei, A Li-rich Layered@Spinel@Carbon heterostructured cathode material for high capacity and high rate lithium-ion batteries fabricated via an in situ synchronous carbonization-reduction method, J. Mater. Chem. 3 (2015) 3995–4003.
[19] F.-D. Yu, L.-F. Que, Z.-B. Wang, Y. Zhang, Y. Xue, B.-S. Liu, D.-M. Gu, Layered-spinel capped nanotube assembled 3D Li-rich hierarchitectures for high performance Li-ion battery cathodes, J. Mater. Chem. 4 (2016) 18416–18425.
[20] Y.P. Deng, Z.W. Yin, Z.G. Wu, S.J. Zhang, F. Fu, T. Zhang, J.T. Li, L. Huang, S.G. Sun, Layered/spinel heterostructured and hierarchical micro/nanostructured Li-rich cathode materials with enhanced electrochemical properties for Li-ion batteries, ACS Appl. Mater. Interfaces 9 (2017) 21065–21070.
[21] Z. Qiu, Y. Zhang, X. Huang, J. Duan, D. Wang, G.P. Nayaka, X. Li, P. Dong, Beneficial effect of incorporating Ni-rich oxide and layered over-lithiated oxide into high-energy-density cathode materials for lithium-ion batteries, J. Power Sources 400 (2018) 341–349.
[22] S. Zhang, J. Chen, T. Tang, Y. Jiang, G. Chen, Q. Shao, C. Yan, T. Zhu, M. Gao, Y. Liu, H. Pan, A novel strategy to significantly enhance the initial voltage and suppress voltage fading of a Li- and Mn-rich layered oxide cathode material for lithium-ion batteries, J. Mater. Chem. 6 (2018) 3610–3624.
[23] P. Hou, L. Xu, J. Song, D. Song, X. Shi, X. Wang, L. Zhang, A high energy density Li-rich positive-electrode material with superior performances via a dual chelating agent co-precipitation route, J. Mater. Chem. 3 (2015) 9427–9431.
[24] J.L. Shi, J.N. Zhang, M. He, X.D. Zhang, Y.X. Yin, H. Li, Y.G. Guo, L. Gu, L.J. Wan, Mitigating voltage decay of Li-rich cathode material via increasing Ni content for lithium-ion batteries, ACS Appl. Mater. Interfaces 8 (2016) 20138–20146.
[25] J. G.F. Kresse, Efficient iterative schemes for ab initio total-energy calculations using a plane-wave basis set, Phys. Rev. B 54 (1996) 11169–11186.
[26] J. G.F. Kresse, Efficiency of ab-initio total energy calculations for metals and semiconductors using a plane-wave basis set, Comput. Mater. Sci. 6 (1996) 36.
[27] P.E. Blöchl, Projector augmented-wave method, Phys. Rev. B 50 (1994) 17953–17979.
[28] D. G.J. Kresse, From ultrasoft pseudopotentials to the projector augmented-wave method, Phys. Rev. B 59 (1999) 18.
[29] J.P. Perdew, K. Burke, M. Ernzerhof, Generalized gradient approximation made simple, Phys. Rev. Lett. 77 (1996) 3865–3868.
[30] H.J. Monkhorst, J.D. Pack, Special points for Brillouin-zone integrations, Phys. Rev. B 13 (1976) 5188–5192.
[31] F. K.I. Momma, VESTA3for three-dimensional visualization of crystal, volumetric and morphology data, J. Appl. Crystallogr. 44 (2011) 1272–1276.
[32] D. Qian, B. Xu, M. Chi, Y.S. Meng, Uncovering the roles of oxygen vacancies in cation migration in lithium excess layered oxides, Phys. Chem. Chem. Phys. 16 (2014) 14665–14668.
[33] F. Wu, Z. Wang, Y. Su, Y. Guan, Y. Jin, N. Yan, J. Tian, L. Bao, S. Chen, Synthesis and characterization of hollow spherical cathode $Li_{1.2}Mn_{0.54}Ni_{0.13}Co_{0.13}O_2$

assembled with nanostructured particles via homogeneous precipitation-hydrothermal synthesis, J. Power Sources 267 (2014) 337–346.
[34] L. Ku, Y. Cai, Y. Ma, H. Zheng, P. Liu, Z. Qiao, Q. Xie, L. Wang, D.-L. Peng, Enhanced electrochemical performances of layered-spinel heterostructured lithium-rich $Li_{1.2}Ni_{0.13}Co_{0.13}Mn_{0.54}O_2$ cathode materials, Chem. Eng. J. 370 (2019) 499–507.
[35] Q. Fu, F. Du, X. Bian, Y. Wang, X. Yan, Y. Zhang, K. Zhu, G. Chen, C. Wang, Y. Wei, Electrochemical performance and thermal stability of $Li_{1.18}Co_{0.15}Ni_{0.15}Mn_{0.52}O_2$ surface coated with the ionic conductor Li_3VO_4, J. Mater. Chem. 2 (2014) 7555–7562.
[36] R. Yu, X. Zhang, T. Liu, L. Yang, L. Liu, Y. Wang, X. Wang, H. Shu, X. Yang, Spinel/layered heterostructured lithium-rich oxide nanowires as cathode material for high-energy lithium-ion batteries, ACS Appl. Mater. Interfaces 9 (2017) 41210–41223.
[37] S. Kim, W. Cho, X. Zhang, Y. Oshima, J.W. Choi, A stable lithium-rich surface structure for lithium-rich layered cathode materials, Nat. Commun. 7 (2016) 13598.
[38] B. Xu, C.R. Fell, M. Chi, Y.S. Meng, Identifying surface structural changes in layered Li-excess nickel manganese oxides in high voltage lithium ion batteries: a joint experimental and theoretical study, Energy Environ. Sci. 4 (2011).
[39] Y. Liu, Z. Yang, J. Li, B. Niu, K. Yang, F. Kang, A novel surface-heterostructured $Li_{1.2}Mn_{0.54}Ni_{0.13}Co_{0.13}O_2$@$Ce_{0.8}Sn_{0.2}O_2$−σ cathode material for Li-ion batteries with improved initial irreversible capacity loss, J. Mater. Chem. 6 (2018) 13883–13893.
[40] J. Han, H. Zheng, Z. Hu, X. Luo, Y. Ma, Q. Xie, D.-L. Peng, G. Yue, Facile synthesis of Li-rich layered oxides with spinel-structure decoration as high-rate cathode for lithium-ion batteries, Electrochim. Acta 299 (2019) 844–852.
[41] Y. Li, Y. Bai, C. Wu, J. Qian, G. Chen, L. Liu, H. Wang, X. Zhou, F. Wu, Three-dimensional fusiform hierarchical micro/nano $Li_{1.2}Ni_{0.2}Mn_{0.6}O_2$ with a preferred orientation (110) plane as a high energy cathode material for lithium-ion batteries, J. Mater. Chem. 4 (2016) 5942–5951.
[42] E. Hu, X. Yu, R. Lin, X. Bi, J. Lu, S. Bak, K.-W. Nam, H.L. Xin, C. Jaye, D.A. Fischer, K. Amine, X.-Q. Yang, Evolution of redox couples in Li- and Mn-rich cathode materials and mitigation of voltage fade by reducing oxygen release, Nat. Energy 3 (2018) 690–698.
[43] J.L. Shi, D.D. Xiao, M. Ge, X. Yu, Y. Chu, X. Huang, X.D. Zhang, Y.X. Yin, X.Q. Yang, Y.G. Guo, L. Gu, L.J. Wan, High-capacity cathode material with high voltage for Li-ion batteries, Adv. Mater. 30 (2018) 1705575.
[44] F.-D.Y.G. Sun, L.-F. Que, L. Deng, M.-J. Wang, Y.-S. Jiang, G. Shao, Z.-B. Wang, Local electronic structure modulation enhances operating voltage in Li-rich cathodes, Nano Energy 66 (2019) 104102.
[45] H.G.J. Hong, S.-K. Jung, K. Ku, K. Kang, Lithium-excess layered cathodes for lithium rechargeable batteries, J. Electrochem. Soc. 162 (2015) A2447–A2467.
[46] B. Li, H. Yan, J. Ma, P. Yu, D. Xia, W. Huang, W. Chu, Z. Wu, Manipulating the electronic structure of Li-rich manganese-based oxide using polyanions: towards better electrochemical performance, Adv. Funct. Mater. 24 (2014) 5112–5118.
[47] Z. Xiao, J. Meng, Q. Li, X. Wang, M. Huang, Z. Liu, C. Han, L. Mai, Novel MOF shell-derived surface modification of Li-rich layered oxide cathode for enhanced lithium storage, Sci. Bull. 63 (2018) 46–53.
[48] X.D. Zhang, J.L. Shi, J.Y. Liang, Y.X. Yin, J.N. Zhang, X.Q. Yu, Y.G. Guo, Suppressing surface lattice oxygen release of Li-rich cathode materials via heterostructured spinel $Li_4Mn_5O_{12}$ coating, Adv. Mater. 30 (2018) 1801751.
[49] H. Wang, Y. Li, Y. Li, Y. Liu, D. Lin, C. Zhu, G. Chen, A. Yang, K. Yan, H. Chen, Y. Zhu, J. Li, J. Xie, J. Xu, Z. Zhang, R. Vila, A. Pei, K. Wang, Y. Cui, Wrinkled graphene cages as hosts for high-capacity Li metal anodes shown by cryogenic electron microscopy, Nano Lett. 19 (2019) 1326–1335.
[50] H. Zhang, T. Yang, Y. Han, D. Song, X. Shi, L. Zhang, L. Bie, Enhanced electrochemical performance of $Li_{1.2}Ni_{0.13}Co_{0.13}Mn_{0.54}O_2$ by surface modification with the fast lithium-ion conductor Li-La-Ti-O, J. Power Sources 364 (2017) 272–279.
[51] P. Hou, J. Yin, M. Ding, J. Huang, X. Xu, Surface/interfacial structure and chemistry of high-energy nickel-rich layered oxide cathodes: advances and perspectives, Small 13 (2017) 1701802.
[52] P. Yan, X. Sun, J. Zheng, X. Cheng, J.-G. Zhang, Tailoring grain boundary structures and chemistry of Ni-rich layered cathodes for enhanced cycle stability of lithium-ion batteries, Nat. Energy 3 (2018) 600–605.
[53] X. Miao, Y. Yan, C. Wang, L. Cui, J. Fang, G. Yang, Optimal microwave-assisted hydrothermal synthesis of nanosized $xLi_2MnO_3{\cdot}(1-x)LiNi_{1/3}Co_{1/3}Mn_{1/3}O_2$ cathode materials for lithium ion battery, J. Power Sources 247 (2014) 219–227.
[54] X. Yu, Y. Lyu, L. Gu, H. Wu, S.-M. Bak, Y. Zhou, K. Amine, S.N. Ehrlich, H. Li, K.-W. Nam, X.-Q. Yang, Understanding the rate capability of high-energy-density Li-rich layered $Li_{1.2}Ni_{0.15}Co_{0.1}Mn_{0.55}O_2$ cathode materials, Adv. Energy Mater. 4 (2014) 1300950.
[55] Y. Li, C. Wu, Y. Bai, L. Liu, H. Wang, F. Wu, N. Zhang, Y. Zou, Hierarchical mesoporous lithium-rich $Li[Li_{0.2}Ni_{0.2}Mn_{0.6}]O_2$ cathode material synthesized via ice templating for lithium-ion battery, ACS Appl. Mater. Interfaces 8 (2016) 18832–18840.
[56] D. Luo, G. Li, C. Fu, J. Zheng, J. Fan, Q. Li, L. Li, A new spinel-layered Li-rich microsphere as a high-rate cathode material for Li-ion batteries, Adv. Energy Mater. 4 (2014) 1400062.